Modulating Single-Atom Palladium Sites with Copper for Enhanced Ambient Ammonia Electrosynthesis

Lili Han[+], Zhouhong Ren[+], Pengfei Ou[+], Hao Cheng, Ning Rui, Lili Lin, Xijun Liu,* Longchao Zhuo, Jun Song,* Jiaqiang Sun, Jun Luo, and Huolin L. Xin*

Abstract: The electrochemical reduction of N_2 to NH_3 is emerging as a promising alternative for sustainable and distributed production of NH_3. However, the development has been impeded by difficulties in N_2 adsorption, protonation of *NN, and inhibition of competing hydrogen evolution. To address the issues, we design a catalyst with diatomic Pd-Cu sites on N-doped carbon by modulation of single-atom Pd sites with Cu. The introduction of Cu not only shifts the partial density of states of Pd toward the Fermi level but also promotes the $d-2\pi^*$ coupling between Pd and adsorbed N_2, leading to enhanced chemisorption and activated protonation of N_2, and suppressed hydrogen evolution. As a result, the catalyst achieves a high Faradaic efficiency of $24.8 \pm 0.8\%$ and a desirable NH_3 yield rate of $69.2 \pm 2.5\,\mu g\,h^{-1}\,mg_{cat.}^{-1}$, far outperforming the individual single-atom Pd catalyst. This work paves a pathway of engineering single-atom-based electrocatalysts for enhanced ammonia electrosynthesis.

Introduction

Ammonia (NH_3) is one of the most highly produced inorganic chemicals in the world because of its vast need in fertilizer production, pharmaceutical production, and many other industrial processes.[1,2] The industrial production of NH_3 commonly relies on the Haber-Bosch process, which requires harsh conditions (350–550°C and 150–350 atm) associated with rather high energy consumption and CO_2 emission.[3–5] Electrochemical N_2 reduction reaction (NRR) to NH_3 is a gentle and ambient process with low energy consumption, considering as a promising alternative to the Haber-Bosch process.[6,7] However, the development of NRR

has been impeded by the lack of efficient electrocatalysts. Single-atom catalysts (SACs) are expected to have great potential to improve the NRR performance due to the lowest site size, nearly 100% atomic efficiency and unique low-coordinated features.[8–11] Many SACs such as Ru,[12,13] Mo,[14] Fe,[15–17] Au,[18] Cu,[19] Y,[20] Ag,[20] and B[21] have been applied for the NRR in aqueous electrolytes.

However, two major challenges associated with the NRR in aqueous media have to be faced.[22] For one thing, to efficiently break N≡N triple bond ($941\,kJ\,mol^{-1}$),[23] an electrocatalyst needs to possess strong N_2 adsorption ability ($* + N_2 \rightarrow *NN$) and low activation energy of the first proton-coupled electron transfer step ($H^+ + e^- + *NN \rightarrow *NNH$).[19,24] For another, most of the protons and electrons in the system go toward the hydrogen evolution reaction (HER) rather than NRR, leading to an extremely low Faradaic efficiency (FE) for NRR under ambient conditions.[25] Therefore, addressing the challenges is critical to purposefully synthesizing active and durable single-atom-based NRR electrocatalysts. Previous studies[22,26] have reported that Pd can form Pd hydrides and promote surface hydrogenation reactions of *NN during NRR, but Pd is subjected to poisoning by molecular hydrogen due to stronger binding to hydrogen adatoms than to nitrogen ones.[27] Cu can not only facilitate the hydrogen dissociation at Pd sites but also enhance the electron transfer rate by strong d-d coupling with Pd toward excellent NRR.[24,27,28] Therefore, incorporation of Cu into single-atom Pd sites is a promising way to modulate the electronic structure of the Pd for NRR, which, however, has not been explored before.

[*] L. L. Han,[+] H. Cheng, Prof. H. L. Xin
Department of Physics and Astronomy, University of California, Irvine
Irvine, CA 92697 (USA)
E-mail: huolin.xin@uci.edu

Z. H. Ren,[+] Dr. X. J. Liu, Prof. J. Luo
Institute for New Energy Materials & Low-Carbon Technologies and Tianjin Key Lab of Photoelectric Materials & Devices, School of Materials Science and Engineering, Tianjin University of Technology
Tianjin 300384 (China)
E-mail: xjliu@tjut.edu.cn

P. F. Ou,[+] J. Song
Department of Mining and Materials Engineering, McGill University
Montreal H3A 0C5 (Canada)
E-mail: jun.song2@mcgill.ca

N. Rui
Chemistry Division, Brookhaven National Laboratory
Upton, NY 11973 (USA)

L. L. Lin
Institute of Industrial Catalysis, College of Chemical Engineering, Zhejiang University of Technology
Hangzhou (China)

Prof. L. C. Zhuo
School of Materials Science and Engineering, Xi'an University of Technology
Xi'an 710048 (China)

J. Q. Sun
State Key Laboratory of Coal Conversion, Institute of Coal Chemistry, Chinese Academy of Sciences
Taiyuan 030001 (China)

[+] These authors contributed equally to this work.

Supporting information and the ORCID identification number(s) for the author(s) of this article can be found under:
https://doi.org/10.1002/anie.202010159.

Inspired by the above breakthroughs and our previous studies about NRR and SACs,[14,15,29] we have rationally modulated single-atom Pd sites and built diatomic Pd-Cu sites on N-doped carbon (PdCu/NC) by the introduction of Cu. The PdCu/NC achieves a high FE of $24.8 \pm 0.8\%$ and a desirable NH_3 yield rate of $69.2 \pm 2.5\ \mu g\,h^{-1}\,mg_{cat.}^{-1}$ at -0.45 V vs. reversible hydrogen electrode (RHE, all potentials in this work are given vs. RHE otherwise stated.) in 0.05 M H_2SO_4, which are 14.6 and 4.2 times of Pd/NC, respectively. Our density functional theory (DFT) calculations reveal that introduction of Cu into Pd/NC not only shifts the partial density of states (pDOS) of Pd toward the Fermi level but also promotes the d-2π* coupling between Pd and adsorbed N_2. It renders N_2 chemisorption, activates hydrogenation of the adsorbed N_2 and suppresses hydrogen evolution, eventually lowering the energy required by the potential-determining step (PDS) to enhance the selectivity of NRR.

Results and Discussion

PdCu/NC was synthesized via a dissolution-and-carbonization method (see Experimental Section in Supporting Information for details). The $Cl_2H_{14}N_4OPd$, $CuCl_2$ and $NH_2OH \cdot HCl$ aqueous solutions were mixed with glucose ethanol solution followed by being dried at 70°C overnight. During this process, the chelated $[NH_3]$ on $Cl_2H_{14}N_4OPd$ can chelate with Cu^{2+} to form a complex of Pd and Cu.[30] Meanwhile, they were efficiently separated by glucose backbones, which ensures a homogeneous distribution of the Pd-Cu active sites in the subsequent calcination. After carbonization at 600°C, the carbon matrix, obtained from carbonization of the glucose, was etched by NH_3 produced via the decomposition of hydroxylamine hydrochloride precursor and formed a 3-dimensional (3D) porous structure.[31] The pyrolyzed metal complexes were transformed into M-N-C sites (M refers to metals).[32] Therefore, Pd-Cu diatomic sites are likely to be formed by the adjacent Pd and Cu atoms, which coordinate with nitrogen and are uniformly dispersed on the 3D carbon matrix. The obtained product was characterized by the high-angle annular dark-field scanning transmission electron microscopy (HAADF-STEM). Figure 1a shows 3D interconnected carbon frameworks with randomly opened porous structure. The N_2 adsorption-desorption isotherm and pore distribution of PdCu/NC in Figure S1 demonstrates the specific area of 214.34 $m^2 g^{-1}$ and the existence of many pores with sizes of 2.3–7 nm. Such pores are beneficial to the exposure of active sites and the mass transport of electrolytes during electrolysis.[14] High-resolution transmission electron microscopy (HRTEM) image and the selected area electron diffraction (SAED) pattern demonstrate the amorphousness of PdCu/NC (Figure 1b and Figure S2a). This finding coincides well with the X-ray diffraction (XRD) results (Figure S2b). Atomic-resolution HAADF-STEM images in Figure 1c show many isolated bright dots distributed on the carbon matrix. When zooming in to the magnified atomic-resolution HAADF-STEM image (Figure 1d), it was found that many atomic pairs with two
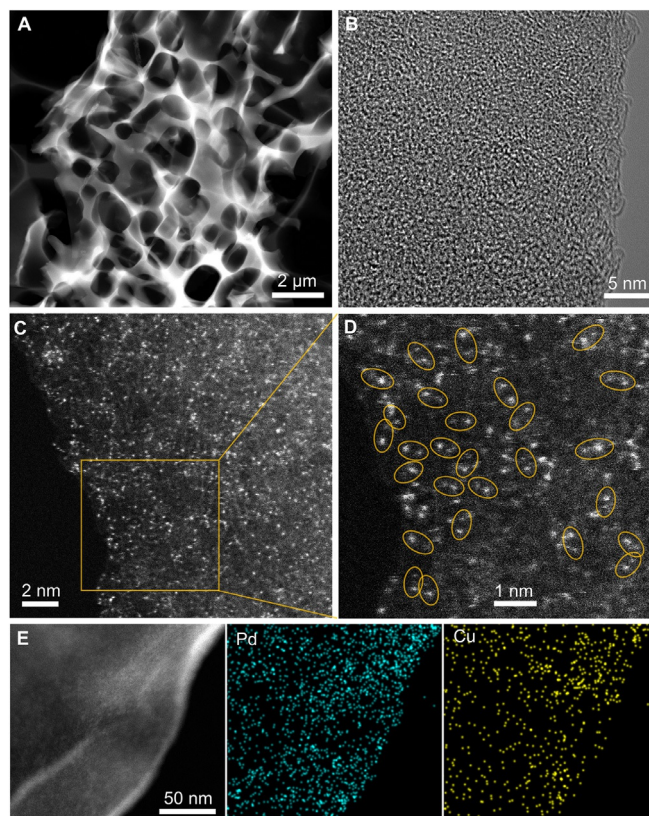

Figure 1. Structural characterizations of PdCu/NC. A) Low-magnification HAADF-STEM image. B) HRTEM image. C) Atomic-resolution HAADF-STEM image. D) Magnified atomic-resolution HAADF-STEM image of the yellow-frame area in (C). Some of atomic pairs are highlighted by yellow oval frames. E) HAADF-STEM image and corresponding EDS mapping images of Pd and Cu.

different contracts were distributed on the carbon matrix. Further, elemental mapping acquired by the energy-dispersive X-ray spectroscopy (EDS) manifests homogeneous distribution of Pd, Cu, N and C over the entire architectures (Figure 1e and Figure S2c), suggesting that the atomic pair is composed of Pd and Cu. The Pd and Cu loadings in PdCu/NC measured by inductively coupled plasma atomic emission spectroscopy (ICP-AES) are 2.23 wt% and 2.32 wt%, respectively.

X-ray absorption fine structure (XAFS) spectroscopy was utilized to explore the local structures of Pd and Cu atoms in PdCu/NC. Figure 2a shows that the Pd X-ray absorption near-edge structure (XANES) edge of PdCu/NC is close to PdO, indicating that the Pd atom valence state is $+2$. Figure 2b presents the Cu K-edge XANES edge of PdCu/NC lies between those of Cu_2O and CuO, indicating that the Cu average valence is between $+1$ and $+2$. The Pd K-edge Fourier transformed extended XAFS (FT-EXAFS) spectrum of PdCu/NC (Figure 2c) displays the main peak at 1.46 Å,[33] which can be attributed to the coordination of Pd to N. The Cu K-edge FT-EXAFS spectrum of PdCu/NC (Figure 2d) displays a main peak at 1.47 Å,[34] which can be assigned to the backscattering of Cu-N coordination.

To determine the structure of PdCu/NC, we established various theoretically optimized models based on DFT (see
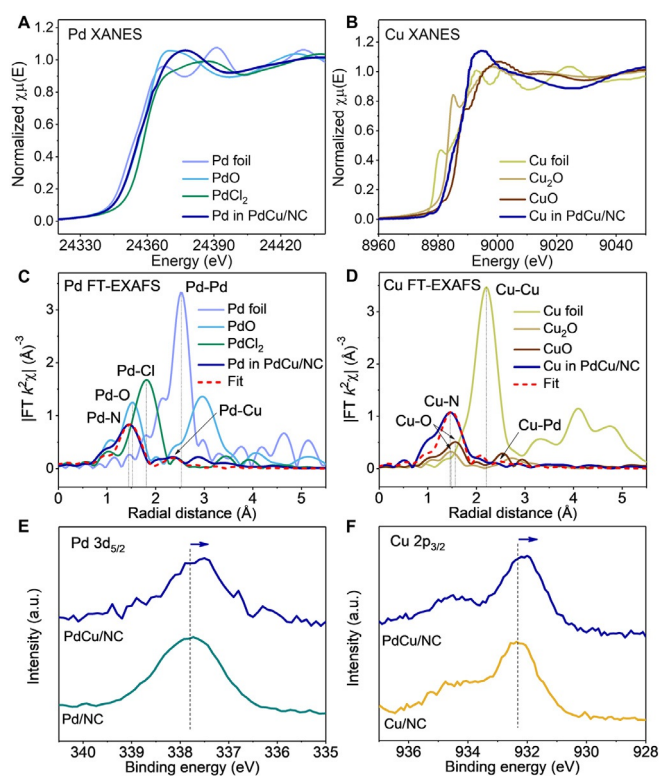
Figure 2. Synchrotron radiation XAFS and XPS measurements. A) Pd K-edge XANES spectra of PdCu/NC and reference samples (Pd foil, PdO, PdCl$_2$). B) Cu K-edge XANES spectra of PdCu/NC and reference samples (Cu foil, Cu$_2$O, CuO). C) Pd K-edge and D) Cu K-edge FT-EXAFS spectra of PdCu/NC and their reference samples. Cu and Pd FT-EXAFS spectra of PdCu/NC were fitted with the PdN$_2$CuN$_2$_556 and PdN$_3$CuN$_3$ mixed configuration. E) Pd 3d XPS spectra of PdCu/NC and Pd/NC. F) Cu 2p XPS spectra of PdCu/NC and Cu/NC.

Computational Section in Supporting Information for more details). Their XANES results were further calculated and shown in Figures S3 and S4, which suggest that the calculated Pd and Cu XANES spectra of PdN$_2$CuN$_2$_556 and PdN$_3$CuN$_3$ structures match well with the experimental ones. Based on the above findings, a fit to the experimental Pd and Cu EXAFS data was performed, and a joint PdN$_2$CuN$_2$_556 and PdN$_3$CuN$_3$ structures in the respective percentage of 65 ± 5 % and 35 ± 5 % was determined (Figure 2 c,d, Figure S5 and Table S1). Such a result is consistent with many Pd, Cu atomic pairs distributed on N-doped carbon in Figure 1 d. To explore the existence of the Pd-Pd and Cu-Cu sites in PdCu/NC, we fitted the Pd and Cu K-edge EXAFS spectra of PdCu/NC using the Pd-Pd (PdN$_2$PdN$_2$_556) and Cu-Cu (CuN$_2$CuN$_2$_556) configuration models. The fitting results in Figure S6 and Table S1 indicate poor fitting qualities (higher R-factor) for both of the two configurations. The finding demonstrates that the neglectable amount of Pd-Pd and Cu-Cu sites formed in PdCu/NC.

Comparison of Pd 3d and Cu 2p X-ray photoelectron spectroscopy (XPS) spectra of PdCu/NC, with those of control samples including Pd/NC and Cu/NC, was performed to explore the electronic structure of PdCu/NC. The Pd/NC and Cu/NC were synthesized via the same method of PdCu/

NC (see Experimental Section in Supporting Information for details). They consist of atomically dispersed Pd and Cu on N-doped carbon, respectively (Figures S7 and S8). The Pd and Cu loadings in Pd/NC and Cu/NC are determined to be 2.94 wt % and 5.53 wt %, respectively, through ICP-AES measurements. Synchrotron radiation XAFS measurements were performed on Cu/NC and Pd/NC samples. Their XANES and EXAFS spectra are shown in Figure S9. We fitted Cu K-edge EXAFS spectra of Cu/NC with CuN$_3$ and Cu-Cu (CuN$_2$CuN$_2$_556) configurations, and fitted Pd K-edge EXAFS spectra of Pd/NC with PdN$_3$ and Pd-Pd (PdN$_2$PdN$_2$_556) configurations. The fitting results are shown in Figure S9c,d and Table S2. The CuN$_3$ and PdN$_3$ configurations show much better fitting qualities (lower R factor and less deviation of fitting coordination numbers from the initial structure models) than the PdN$_2$PdN$_2$ and CuN$_2$CuN$_2$ configurations, suggesting that CuN$_3$ and PdN$_3$ are dominant sites in Cu/NC and Pd/NC. Figure 2 e,f displays that Pd 3d$_{5/2}$ and Cu 2p$_{3/2}$ XPS peaks in PdCu/NC shift by −0.15 eV and −0.16 eV compared with the Pd one in Pd/NC and the Cu one in Cu/NC, respectively, which suggests that both Cu and Pd in PdCu/NC lose fewer electrons than Pd in Pd/NC and Cu in Cu/NC, respectively. This finding is consistent with the charge calculation result, where Pd in PdCu/NC and Cu in PdCu/NC have 0.154 and 0.091 electrons more than Pd in Pd/NC and Cu in Cu/NC, respectively (Figure S10). On the contrary, C 1s peak of PdCu/NC has no shift compared to those of Pd/NC and Cu/NC (Figure S11). These comparisons demonstrate that the introduction of the SA Cu into the SA Pd has a great effect on the electronic structures of both the Cu and the Pd, which suggests the bonding of Cu and Pd in PdCu/NC. The finding aligns well with the XAFS result that PdCu/NC is composed of the mixed PdN$_2$CuN$_2$_556 and PdN$_3$CuN$_3$ structures.

The NRR performance of the PdCu/NC catalyst was examined in N$_2$-saturated 0.05 M H$_2$SO$_4$ under ambient conditions according to our previous work[14,15] (see Experimental Section in Supporting Information for more details). To exclude the possible contaminants of NH$_3$ and NO$_x$ in the feeding gases, N$_2$ and Ar gases were purified by 2 M NaOH, 0.1 M FeSO$_4$ and 5 mM H$_2$SO$_4$ solutions.[35] The NH$_3$ yield rates were estimated by the indophenol blue method.[36] As shown in Figure 3a, the NH$_3$ yields over the PdCu/NC electrocatalyst increase with more negative potential until reaching −0.45 V, where the maximum value of NH$_3$ yield rate is calculated as 69.2 ± 2.5 µg h^{-1} mg$_{cat.}$$^{-1}$, 4.2 and 3.0 times of Pd/NC and Cu/NC, respectively. It achieved the maximum FE of 24.8 ± 0.8 % at −0.45 V, 14.6 and 3.6 times of Pd/NC and Cu/NC, respectively (Figure 3b). These results demonstrate that the PdCu/NC is far more selective and active than Pd/NC for NRR to NH$_3$.

To confirm the origin of the NH$_3$ produced, the controlled experiments and isotope measurements were performed.[35] As shown in Figure 3c, no NH$_3$ was detected after NRR experiments performed over the PdCu/NC catalyst for 2 h in Ar-saturated catholyte, solely on carbon paper, and in the N$_2$-saturated electrolyte without electrolysis (that is, open circuit). Moreover, the ^{15}N isotopic labeling experiment (Figure 3d) demonstrated a triplet coupling for ^{14}NH$_4$$^+$ and
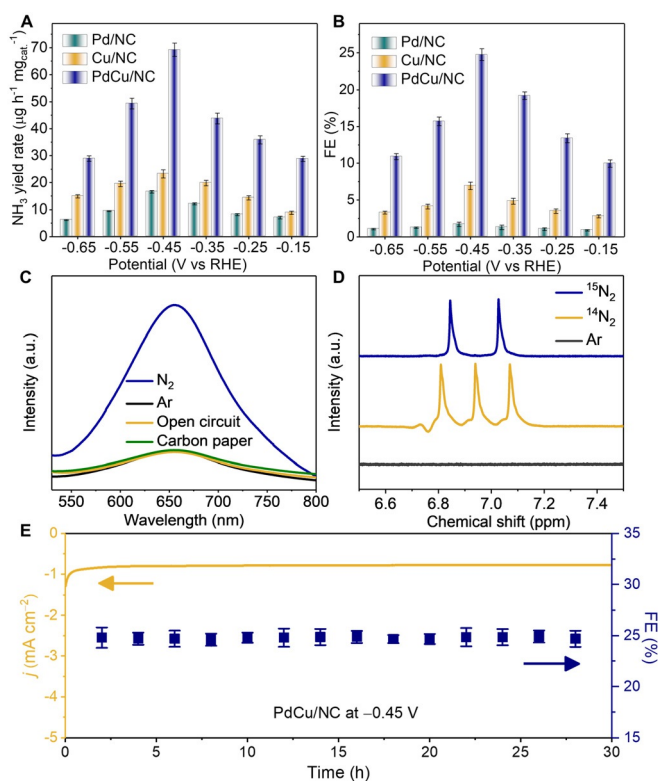
Figure 3. NRR performances. A) NH_3 yield rates and B) FEs of PdCu/NC, Pd/NC, and Cu/NC at each given potential in N_2-saturated 0.05 M H_2SO_4. C) UV-vis absorption spectra of electrolytes stained with indophenol blue indicator after NRR on PdCu/NC, carbon paper, Ar control experiment, and open circuit condition at −0.45 V. D) ^{1}H NMR spectra of 0.05 M H_2SO_4 solutions after 2 h of electrochemical reduction on PdCu/NC at −0.45 V using Ar (black), $^{14}N_2$ (yellow) and $^{15}N_2$ (blue) as the feeding gases. E) Chronoamperometric curve and FE stabilities of PdCu/NC during 30 h of electrolysis.

a double coupling for $^{15}NH_4^+$. The isotopic ^{15}N measurement result for the quantification of ammonia shows that the concentration of $^{15}NH_4^+$ product after $^{15}N_2$ reduction was determined to be 51.2 μM (Figure S12), close to the value (50.9 μM) measured by the indophenol blue method. More importantly, the two values are in the range of (50.7 ± 1.8 μM) measured by performing the electrocatalysis of $^{14}N_2$ (Figure 3a). These confirm that the generated ammonia is produced from the NRR. In addition, stability is a critical parameter of NRR performance for practical applications. Under sustained N_2 gas flow, 30-h electrolysis on the PdCu/NC catalyst at a potential of −0.45 V only leads to a slight decrease in current density and NH_3 yield rate (Figure 3e), indicating that the high stability of PdCu/NC for NRR. Additional XRD, HAADF-STEM and electrochemical impedance spectroscopy (EIS) characterizations further confirmed the stability of PdCu/NC (Figure S13).

To better understand the observations and provide theoretical insights, DFT calculations were performed on the PdCu/NC, Pd/NC and Cu/NC systems to examine their respective catalytic activity and selectivity for NRR (see Computational Section in Supporting Information for more details). In particular, based on the EXAFS fitting results in

Figure 2c,d, we built the PdN_3CuN_3 and the $PdN_2CuN_2\_556$ models for the PdCu/NC system, and the CuN_4, PdN_4, CuN_3 and PdN_3 models for the reference Pd/NC and Cu/NC systems (Figure S14). Then, N_2 adsorption on different models was investigated, as adequate N_2 adsorption and activation are the prerequisites for an efficient NRR process.[9,37] Figure S14a compares PdN_3CuN_3 with PdN_4 and CuN_4 in their interaction with N_2, showing that they all weakly interact with N_2 and fail to chemically adsorb and activate the inert triple bond of N_2. This is consistent with the previous theoretical studies,[19,37] indicating that PdN_4 or CuN_4 structures are not suitable catalyst candidates for NRR. This finding also suggests that the active sites of the PdCu/NC catalyst for NRR are not from the PdN_3CuN_3 structure.

Meanwhile, Figure S14b shows the case of $PdN_2CuN_2\_556$ in comparison with PdN_3 and CuN_3, demonstrating that N_2 can be only physisorbed on the sites of PdN_3 and CuN_3 via the end-on configuration with weak binding strength, with the free-energy changes of N_2 adsorption (ΔG_{*N_2}) being 0.46 eV and −0.05 eV respectively. The weakly adsorbed N_2 exhibits a bond length similar to that of its gas-phase (1.11 Å, Figure S14a), signaling failure to activate the inert triple bond of N_2, hence preventing the reaction from proceeding to the subsequent NRR steps. On the other hand, $PdN_2CuN_2\_556$ shows strong interaction with N_2, leading to considerably elongated N≡N triple bond lengths of 1.17 and 1.15 Å for the side-on and end-on configurations (Figure S14b), respectively. The elongation significantly weakens the N≡N triple bond to yield chemisorption with much larger ΔG_{*N_2} values of −0.71 eV and −0.58 eV. The result suggests the $PdN_2CuN_2\_556$ structure to be the responsible active center on the PdCu/NC catalyst to facilitate NRR. In the following, for simplicity of the discussion, PdCu/NC, Pd/NC and Cu/NC are represented by the $PdN_2CuN_2\_556$, PdN_3 and CuN_3, respectively.

The above results highlight that weakening of the triple bond and chemical bonding formation of N_2 on PdCu/NC together contribute obvious activation of N_2 that is beneficial for the subsequent NRR steps. To further analyze the interactions between the adsorbed N_2 and metals and understand the underlying mechanism of N_2 activation on the PdCu/NC, we examined the pDOS and projected crystal orbital Hamilton population (pCOHP).[38] From the pDOSs in Figure 4a, the introduction of Cu into Pd/NC moves the pDOS of Pd 4d toward more positive values, and consequently, more pDOSs of Pd 4d are involved in the overlap region with those of N 2p near the Fermi level. Additionally, from the computed −pCOHP as shown in Figure 4b, the capability of PdCu/NC to adsorb and activate N_2 is ascribed to two aspects: the 2π and 3σ molecular orbitals of N_2 donate electrons to the unoccupied d orbitals of Pd and Cu to form the bonding states to strengthen the N_2 adsorption. Moreover, we note that the appearance of occupied 2π* molecular orbitals near the Fermi level for PdCu/NC, that is, the occupied d orbitals of Pd and Cu back-donate electrons to the 2π* molecular orbitals of N_2 to activate N_2 hydrogenation.[10] This further distinguishes PdCu/NC from the Pd/NC and the Cu/NC systems. For a more quantitative analysis, the integrated pCOHP (ICOHP) (Figure 4b) was also computed to
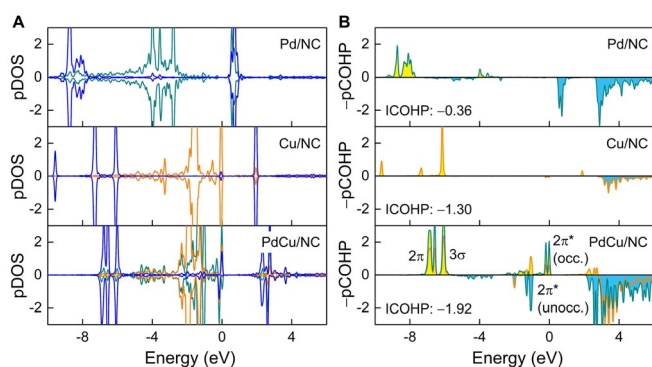
Figure 4. Computed electronic properties for Pd/NC, Cu/NC, and PdCu/NC, represented by PdN₃, CuN₃, and PdN₂CuN₂_556, respectively. A) Partial density of states (pDOS) of N₂ adsorption on Pd/NC, Cu/NC, and PdCu/NC. Blue lines: 2p orbital of N, orange lines: 3d orbital of Cu, and cyan lines: 4d orbital of Pd. B) Projected crystal orbital Hamilton population (−pCOHP) and its integrated value (ICOHP) of N₂ adsorption on Pd/NC, Cu/NC, and PdCu/NC. Orange and cyan lines indicate the bondings between N-Cu and N-Pd. The energy value is with reference to the Fermi level.

compare the d-2π* coupling PdCu/NC with Pd/NC and Cu/NC. From the Figure, a more negative ICOHP was observed for PdCu/NC, indicating a much stronger d-2π* coupling.

In terms of the subsequent NRR steps, the protonation of adsorbed *N₂ (*N₂ + (H⁺ + e⁻) → *NNH) is the PDS in both distal and alternating pathways for Pd/NC and Cu/NC. The *NNH formation exhibits huge ΔG_{PDS} values for Pd/NC and Cu/NC, being 1.31 eV and 1.85 eV respectively, effectively rendering them NRR inactive (Figure 5a,b). Considering the intensive energy demand of *N₂H₂ formation (0.72 and 0.74 eV) in the distal pathway for Pd/NC and Cu/NC, the

alternating pathway is more energetically favorable on these single-atom sites. In contrast, PdCu/NC shows a much lower the free-energy change for the *NNH formation (ΔG_{*NNH}), i.e., 0.67 eV, thus demonstrating a substantial enhancement in catalytic activity compared to Pd/NC and Cu/NC. As a result of a much reduced ΔG_{*NNH}, the PDS on PdCu/NC is changed from *NNH formation to the protonation of *NH₂ (*NH₂ + (H⁺ + e⁻) → *NH₃, 0.78 eV), as shown in Figure 5c. Additionally, it is worth mentioning that PdCu/NC favors the distal pathway energetically, different from Pd/NC and Cu/NC which would prefer the alternating pathway.
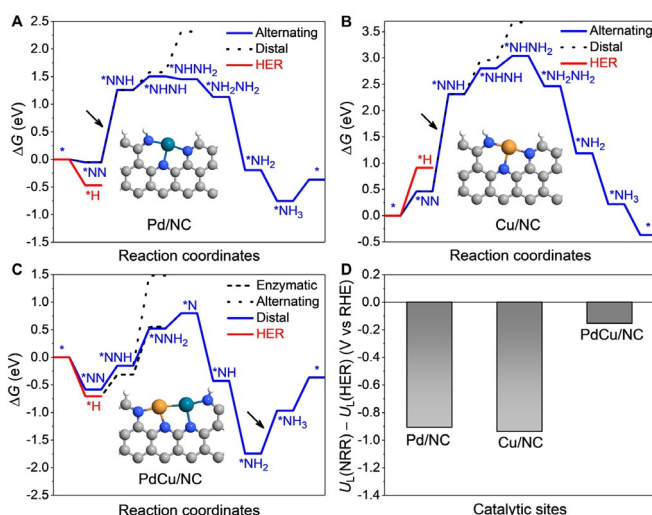
Furthermore, the selectivity of Pd/NC, Cu/NC and PdCu/NC is also quantified by computing the difference between thermodynamic limiting potentials for NRR and HER (i.e., $U_L(NRR)−U_L(HER)$, where U_L is the minimum potential that required for all reaction steps being downhill in free-energies).[39,40] The results are summarized in Figure 5d, along with calculated ΔG_{*H} for HER presented in Figure 5a–c. For PdCu/NC, the $U_L(NRR)−U_L(HER)$ value (−0.15 V) is more positive than those for Pd/NC (−0.91 V) and Cu/NC (−0.94 V), indicating higher selectivity for NRR and inhibition of the competing HER. Collectively, the enhanced catalytic performance of PdCu/NC for NRR results from enhanced N₂ adsorption, a different reaction mechanism with reduced ΔG_{PDS}, as well as the suppression of HER.

Conclusion

In summary, the incorporation of Cu into single-atom Pd sites to form diatomic Pd-Cu sites on N-doped carbon is designed and synthesized as an NRR electrocatalyst. Consequently, the FE and the yield rate of NH₃ are substantially higher than the counterpart values of individual single-atom Pd catalyst. Our DFT calculations reveal that the introduction of Cu into Pd/NC not only moves the pDOS of Pd toward the Fermi level but also promotes the d-2π* coupling between Pd and adsorbed N₂. This renders N₂ chemisorption and activates the adsorbed N₂ to be hydrogenation, which result in lowered energy required by the potential-determining step and eventually enhanced selectivity of NRR to NH₃. These findings may further inspire the design of efficient single-atom-based electrocatalysts toward NRR.

Figure 5. Reaction activity and selectivity from DFT calculations. Calculated free-energy diagrams of NRR and HER on A) Pd/NC, B) Cu/NC, and C) PdCu/NC systems. The alternating pathway is favored on Pd/NC and Cu/NC, whereas the distal pathway is the most energetically preferred on PdCu/NC. The asterisk (*) represents a reactive intermediate or a vacant surface site. Insets: structural models. D) Difference between the limiting potentials for NRR and HER of Pd/NC, Cu/NC, and PdCu/NC.

Angew. Chem. Int. Ed. **2021**, 60, 345–350

© 2020 Wiley-VCH GmbH

www.angewandte.org **349**

Conflict of interest

The authors declare no conflict of interest.

[1] Y. Zhao, Y. Zhao, R. Shi, B. Wang, G. I. N. Waterhouse, L.-Z. Wu, C.-H. Tung, T. Zhang, *Adv. Mater.* **2019**, *31*, 1806482.

[2] H. Cheng, L.-X. Ding, G.-F. Chen, L. Zhang, J. Xue, H. Wang, *Adv. Mater.* **2018**, *30*, 1803694.

[3] G. F. Chen, S. Ren, L. Zhang, H. Cheng, Y. Luo, K. Zhu, L. X. Ding, H. Wang, *Small Methods* **2019**, *3*, 1800337.

[4] X. Ren, J. Zhao, Q. Wei, Y. Ma, H. Guo, Q. Liu, Y. Wang, G. Cui, A. M. Asiri, B. Li, B. Tang, X. Sun, *ACS Cent. Sci.* **2019**, *5*, 116–121.

[5] Z. Wang, F. Gong, L. Zhang, R. Wang, L. Ji, Q. Liu, Y. Luo, H. Guo, Y. Li, P. Gao, X. Shi, B. Li, B. Tang, X. Sun, *Adv. Sci.* **2019**, *6*, 1801182.

[6] C. Zhao, S. Zhang, M. Han, X. Zhang, Y. Liu, W. Li, C. Chen, G. Wang, H. Zhang, H. Zhao, *ACS Energy Lett.* **2019**, *4*, 377–383.

[7] L. Zhang, L. X. Ding, G. F. Chen, X. Yang, H. Wang, *Angew. Chem. Int. Ed.* **2019**, *58*, 2612–2616; *Angew. Chem.* **2019**, *131*, 2638–2642.

[8] X. Liu, Y. Jiao, Y. Zheng, M. Jaroniec, S. Z. Qiao, *J. Am. Chem. Soc.* **2019**, *141*, 9664–9672.

[9] J. Zhao, Z. Chen, *J. Am. Chem. Soc.* **2017**, *139*, 12480–12487.

[10] X. Guo, J. Gu, S. Lin, S. Zhang, Z. Chen, S. Huang, *J. Am. Chem. Soc.* **2020**, *142*, 5709–5721.

[11] X. Guo, S. Huang, *Electrochim. Acta* **2018**, *284*, 392–399.

[12] H. Tao, C. Choi, L.-X. Ding, Z. Jiang, Z. Han, M. Jia, Q. Fan, Y. Gao, H. Wang, A. W. Robertson, S. Hong, Y. Jung, S. Liu, Z. Sun, *Chem* **2019**, *5*, 204–214.

[13] Z. Geng, Y. Liu, X. Kong, P. Li, K. Li, Z. Liu, J. Du, M. Shu, R. Si, J. Zeng, *Adv. Mater.* **2018**, *30*, 1803498.

[14] L. Han, X. Liu, J. Chen, R. Lin, H. Liu, F. Lü, S. Bak, Z. Liang, S. Zhao, E. Stavitski, J. Luo, R. R. Adzic, H. L. Xin, *Angew. Chem. Int. Ed.* **2019**, *58*, 2321–2325; *Angew. Chem.* **2019**, *131*, 2343–2347.

[15] F. Lü, S. Zhao, R. Guo, J. He, X. Peng, H. Bao, J. Fu, L. Han, G. Qi, J. Luo, X. Tang, X. Liu, *Nano Energy* **2019**, *61*, 420–427.

[16] M. Wang, S. Liu, T. Qian, J. Liu, J. Zhou, H. Ji, J. Xiong, J. Zhong, C. Yan, *Nat. Commun.* **2019**, *10*, 341.

[17] J. Li, S. Chen, F. Quan, G. Zhan, F. Jia, Z. Ai, L. Zhang, *Chem* **2020**, *6*, 1–17.

[18] Q. Qin, T. Heil, M. Antonietti, M. Oschatz, *Small Methods* **2018**, *2*, 1800202.

[19] W. Zang, T. Yang, H. Zou, S. Xi, H. Zhang, X. Liu, Z. Kou, Y. Du, Y. P. Feng, L. Shen, L. Duan, J. Wang, S. J. Pennycook, *ACS Catal.* **2019**, *9*, 10166–10173.

[20] Y. Chen, R. Guo, X. Peng, X. Wang, X. Liu, J. Ren, J. He, L. Zhuo, J. Sun, Y. Liu, Y. Wu, J. Luo, *ACS Nano* **2020**, *14*, 6938–6946.

[21] C. Ling, X. Niu, Q. Li, A. Du, J. Wang, *J. Am. Chem. Soc.* **2018**, *140*, 14161–14168.

[22] J. Wang, L. Yu, L. Hu, G. Chen, H. Xin, X. Feng, *Nat. Commun.* **2018**, *9*, 1795.

[23] H. Huang, F. Gong, Y. Wang, H. Wang, X. Wu, W. Lu, R. Zhao, H. Chen, X. Shi, A. M. Asiri, T. Li, Q. Liu, X. Sun, *Nano Res.* **2019**, *12*, 1093–1098.

[24] W. Tong, B. Huang, P. Wang, L. Li, Q. Shao, X. Huang, *Angew. Chem. Int. Ed.* **2020**, *59*, 2649–2653; *Angew. Chem.* **2020**, *132*, 2671–2675.

[25] X. Cui, C. Tang, Q. Zhang, *Adv. Energy Mater.* **2018**, *8*, 1800369.

[26] G. Deng, T. Wang, A. A. Alshehri, K. A. Alzahrani, Y. Wang, H. Ye, Y. Luo, X. Sun, *J. Mater. Chem. A* **2019**, *7*, 21674–21677.

[27] M.-M. Shi, D. Bao, S.-J. Li, B.-R. Wulan, J.-M. Yan, Q. Jiang, *Adv. Energy Mater.* **2018**, *8*, 1800124.

[28] F. Pang, Z. Wang, K. Zhang, J. He, W. Zhang, C. Guo, Y. Ding, *Nano Energy* **2019**, *58*, 834–841.

[29] L. Han, S. Song, M. Liu, S. Yao, Z. Liang, H. Cheng, Z. Ren, W. Liu, R. Lin, G. Qi, X. Liu, Q. Wu, J. Luo, H. Xin, *J. Am. Chem. Soc.* **2020**, *142*, 12563–12567.

[30] K. Eskandari, F. Ebadinejad, *Mol. Phys.* **2018**, *116*, 1369–1376.

[31] H. Liang, X. Zhuang, S. Brüller, X. Feng, K. Müllen, *Nat. Commun.* **2014**, *5*, 4973.

[32] P. Li, Z. Jin, Y. Qian, Z. Fang, D. Xiao, G. Yu, *ACS Energy Lett.* **2019**, *4*, 1793–1802.

[33] S. Zhou, L. Shang, Y. Zhao, R. Shi, G. I. N. Waterhouse, Y.-C. Huang, L. Zheng, T. Zhang, *Adv. Mater.* **2019**, *31*, 1900509.

[34] H. Yang, H. Wu, G. Li, Q. Lin, Q. Hu, Q. Zhang, J. Liu, C. He, *J. Am. Chem. Soc.* **2019**, *141*, 12717–12723.

[35] S. Z. Andersen, V. Čolić, S. Yang, J. A. Schwalbe, A. C. Nielander, J. M. McEnaney, K. Enemark-Rasmussen, J. G. Baker, A. R. Singh, B. A. Rohr, M. J. Statt, S. J. Blair, S. Mezzavilla, J. Kibsgaard, P. C. K. Vesborg, M. Cargnello, S. F. Bent, T. F. Jaramillo, I. E. L. Stephens, J. K. Nørskov, I. Chorkendorff, *Nature* **2019**, *570*, 504–508.

[36] D. Zhu, L. Zhang, R. E. Ruther, R. J. Hamers, *Nat. Mater.* **2013**, *12*, 836–841.

[37] C. Ling, Y. Ouyang, Q. Li, X. Bai, X. Mao, A. Du, J. Wang, *Small Methods* **2019**, *3*, 1800376.

[38] S. Maintz, V. L. Deringer, A. L. Tchougréeff, R. Dronskowski, *J. Comput. Chem.* **2016**, *37*, 1030–1035.

[39] D. Kim, C. Xie, N. Becknell, Y. Yu, M. Karamad, K. Chan, E. J. Crumlin, J. K. Nørskov, P. Yang, *J. Am. Chem. Soc.* **2017**, *139*, 8329–8336.

[40] C. Shi, H. A. Hansen, A. C. Lausche, J. K. Nørskov, *Phys. Chem. Chem. Phys.* **2014**, *16*, 4720–4727.

350   www.angewandte.org

© 2020 Wiley-VCH GmbH

Angew. Chem. Int. Ed. **2021**, *60*, 345–350